# Scheme for Majorana Manipulation in Topological Superconductors Using Magnetic Force Microscopy

Benjamin H. November,[1] Jay D. Sau,[2,*] James R. Williams,[3] and Jennifer E. Hoffman[1,4,†]

[1] *Department of Physics, Harvard University, Cambridge, Massachusetts 02138, USA*
[2] *Condensed Matter Theory Center and Joint Quantum Institute, Department of Physics, University of Maryland, College Park, Maryland 20742, USA*
[3] *Joint Quantum institute, Center for Nanophysics and Advanced Materials, Department of Physics, University of Maryland, College Park, Maryland 20742, USA*
[4] *School of Engineering & Applied Sciences, Harvard University, Cambridge, Massachusetts 02138, USA*

(Dated: June 14, 2023)

We suggest a scheme for the use of magnetic force microscopy (MFM) to manipulate and measure Majorana zero modes emergent in vortex cores of topological superconductors. We calculate the energy splitting and the resulting change in charge and current density around the vortex cores due to the overlap of the Majorana wavefunctions when a composite fermion is formed. The corresponding excess magnetic field gradient above the vortex background can be measured by MFM, constituting a readout of Majorana pair parity. This Majorana parity signal can then be used to measure the expected lifetime of the topologically protected quantum information in the system.

1 *Introduction.*—The primary obstacle to achieving scalable quantum computation is the vulnerability of qubits to environmental perturbation. To this end, there has been a strong push for the investigation of topological quantum computation (TQC) where protection from local fluctuations derives from the non-local nature of the qubit states, greatly increasing their stability [1]. Majoranas, emergent excitations that satisfy non-abelian exchange statistics, have been suggested as components of a topological qubit [2]. However, success of this approach requires a method to store and read out the information in the parity of a pair of Majoranas after an exchange. When two Majoranas are contracted to single point, they can either annihilate or form a canonical fermion [3, 4]. The quantum information stored in the pair is the presence or absence of the charged fermion, so measurement of the increased charge or current density would constitute a readout of the parity of the Majorana pair. It is thus possible to use the braiding statistics and non-locality of Majorana states to create perturbation-resistant qubits.

2 Previous experiments have focused primarily on Majoranas at the edges of semiconductor nanowires on a superconducting substrate [5, 6], where there has been some hard-won progress; however, tight constraints on temperature, magnetic field, and interface quality remain challenging. Majoranas may also be found in single materials where bulk $s$-wave superconductivity can self-proximitize the helical surface states, creating an effective topological superconductor on the surface [7]. Vortex cores in these systems are predicted to host zero energy bound states with Majorana exchange statistics, known as Majorana zero modes (MZMs) [8–10]. Scanning tunneling microscopy (STM) experiments have observed zero bias conductance peaks (ZBCPs) suggestive of MZMs in the vortex cores of several Fe-based superconductors, including $FeTe_{0.55}Se_{0.45}$ [11–14], $(Li_{0.84}Fe_{0.16})OHFeSe$ [15], $CaKFe_4As_4$ [16], and LiFeAs [17].

3 The ZBCP can be distinguished from the conventional Caroli-deGennes-Matricon (CdGM) subgap states of the vortex in several materials. CdGM states scale as $\pm\Delta^2/E_F$, where $\Delta$ is the superconducting gap and $E_F$ is the chemical potential [18]. $FeTe_{0.55}Se_{0.45}$ is among the primary candidates to utilize MZMs, due to its relatively large $\Delta = 1.8$ meV and small $E_F = 4.4$ meV with respect to the Dirac point [11], yielding a sufficiently large spectral gap between CdGM states, such that an isolated ZBCP within can be easily distinguished by STM measurements at dilution fridge temperatures (Section I in [19]). $FeTe_{0.55}Se_{0.45}$ can thus host topologically protected qubits, but a scheme for the readout and manipulation of these qubits is still lacking.

4 Here we develop a general scheme for braiding MZMs in topological superconductors with vortex manipulation and parity readout via magnetic force microscopy (MFM). We propose to first detect the MZMs in vortex cores by tunneling measurement of a ZBCP, then manipulate the vortex by magnetic force coupling between the vortex and the MFM tip. While vortices have been shown to couple to locally applied mechanical [20], thermal [21], and magnetic SQUID [22] probes, the higher spatial resolution along with the tunneling capabilities of MFM allow for simultaneous identification and manipulation of MZMs, as well as sensitivity to local magnetic fields required for readout of MZM pair parity. Additionally, MFM can be operated using a large tip-sample separation during vortex manipulation to reduce quasiparticle poisoning, and then can rapidly approach the tip towards a pair of assembled MZMs to make a parity readout. We quantify the feasibility to detect the resultant MZM parity by magnetic force readout for the specific material $FeTe_{0.55}Se_{0.45}$. By repeated measurements, the Majorana parity lifetime could also be quantified, and ultimately more complex braiding could be used to conduct

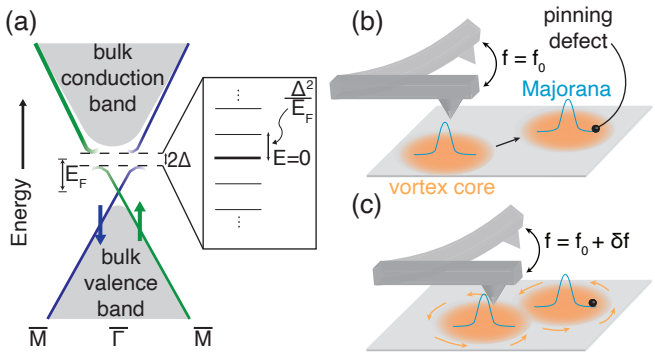


FIG. 1. (a) Surface band structure schematic, supported by ARPES [23]. Inset shows the ladder of subgap states with a true zero mode (thick line) and trivial CdGM modes (thin lines) separated by $\Delta^2/E_F$ [18]. (b-c) Schematic of Majorana parity readout process. (b) MFM cantilever tip is used to bring one vortex close to another pinned vortex, causing the MZMs to overlap. (c) When in the parity 1 state, as shown here, the MZMs form a canonical fermion, generating an excess current density (orange arrows), and a corresponding change in cantilever resonance frequency $\delta f$, above the background (parity 0 state).

logical operations.

5 $FeTe_{0.55}Se_{0.45}$ exhibits bulk $s$-wave superconductivity up to $T_c = 14.5$ K [24, 25]. However, ARPES studies also find a Dirac cone [23] in the bulk band structure, emerging from inversion between an odd-parity $p$ band and an even parity $d$ band along the $\Gamma$-$Z$ direction [26]. Cooper pairs are free to tunnel between any of the pockets in the Brillouin zone to the surface states, leading to an effective internal proximity effect from the bulk into the topological surface states. Therefore, $FeTe_{0.55}Se_{0.45}$ realizes the Fu-Kane model for proximity-induced $s$-wave superconductivity on topologically protected surface states [7].

6 We seek to address how to measure the quantum state of a pair of MZMs in two distinct vortices. Each Majorana operator $\gamma_{j=1,2}$ associated with these MZMs can be considered half a fermionic operator such that the combination $c^\dagger = \gamma_1 + i\gamma_2$ is a canonical fermion creation operator [3, 4]. The MZMs are fused by bringing the pair of vortices together to within a coherence length so their cores overlap. The fermionic occupation $c^\dagger c$ of the overlapping MZM pair then determines the presence or absence of an excess quasiparticle, which would give rise to an excess charge and current density above the background of the fused vortices.

7 First, we will consider the limit where a pair of vortices are brought to completely overlap so that they fuse into a double flux quantum vortex. In this limit, polar symmetry reduces the problem to solving for the low energy eigenstates of the 1-D radial Bogoliubov-de-Gennes (BdG) equation. Second, we will inspect the case of two spatially separated single flux quantum vortices by discretizing the surface Hamiltonian and solving the BdG equation on a grid. We refer to these methods for solving the BdG equation as the continuum and lattice models, respectively. We can check the discretization error of the lattice model through comparison to the continuum model in the double flux quantum vortex limit. In both models, the occupancy of the lowest energy solution measures the quantum state of the composite fermion formed by the overlap of the MZM pair.

8 *Continuum Model - Double Vortex*—A vortex state can be described by the BdG Hamiltonian:

$$H = [v\boldsymbol{\sigma}\cdot\boldsymbol{p} - E_F]\tau_z + [\Delta(\mathbf{r})\tau_+ + h.c], \tag{1}$$

where $\boldsymbol{p}$ is the momentum operator of the topologically-protected surface state, $v$ is the Fermi velocity, $E_F$ is the chemical potential, and $\boldsymbol{\tau}$ and $\boldsymbol{\sigma}$ are the Pauli matrices in Nambu and spin space, respectively [7, 27]. In polar coordinates, the gap is taken to be of the conventional form $\Delta(\boldsymbol{r}/\xi) = \Delta(r/\xi)e^{in\theta} = \Delta_0\tanh(r/\xi)e^{in\theta}$, where $\xi$ is the coherence length, $\Delta_0$ is the magnitude of the superconducting gap, and $n$ is the winding number of the vortex. The Hamiltonian becomes

$$H = -i\hbar v\left[(\sigma_x\cos\theta + \sigma_y\sin\theta)\partial_r + \frac{1}{r}(\sigma_y\cos\theta - \sigma_x\sin\theta)\partial_\theta\right]\tau_z - E_F\tau_z + \Delta(r)\left[\cos(n\theta)\tau_x + \sin(n\theta)\tau_y\right]. \tag{2}$$

Eq. 2 commutes with the total angular momentum operator and can thus be simplified by the appropriate choice of unitary transformation to the radial BdG equation given by

$$\Big[-i\hbar v\sigma_x\tau_z\partial_r + \tau_z\Big(E_F - \frac{\hbar v}{2r}\sigma_y(\sigma_z + n\tau_z - 2m)\Big) + \Delta(r)\tau_x - E\Big]\Psi(r) = 0. \tag{3}$$

where $m$ is the angular momentum quantum number of the vortex. We choose to work in units where $\hbar = v = \Delta_0 = 1$, forcing $\xi = 1$ and $\Delta(r) = \tanh(r)$. By rotating $\sigma_x \to \sigma_y$ about the $z$ axis, the BdG equation becomes real and 1-D, given by

$$\Big[\partial_r - \Big(iE_F\sigma_y - \frac{1}{2r}(1 + \sigma_z(n\tau_z - 2m))\Big) - \tanh(r)\tau_y\sigma_y - iE\sigma_y\tau_z\Big]\Psi(r) = 0. \tag{4}$$

9 We seek the lowest energy solution $\Psi(r)$, for $m = \frac{1}{2}$ where a zero-energy solution exists for a double flux quantum vortex ($n = 2$) (Sections II-III in [19]). Though the system was solved analytically for $E_F = 0$ [7, 28], here we solve Eq. 4 for the more realistic condition $E_F/\Delta = 2.5$, comparable to the measured value for $FeTe_{0.55}Se_{0.45}$ [11]. The occupation of the state $\Psi(r)$ is associated with a corresponding excess charge and current density above the background of the double flux quantum vortex, shown

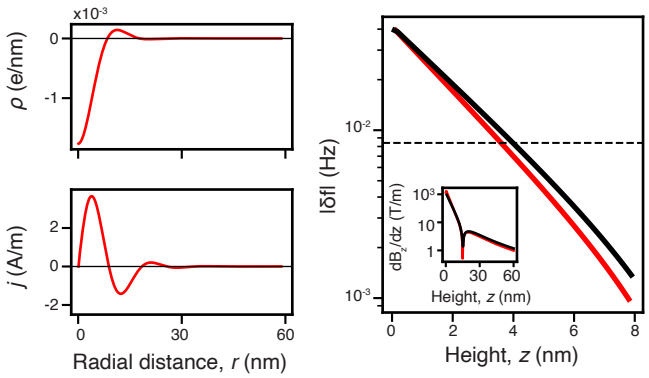


FIG. 2. (a) Excess charge density associated with the lowest energy wavefunction of a double flux quantum vortex as a function of the lateral distance $r$ from the vortex center, calculated in the continuum model. (b) Excess surface current density for the same state. For this calculation $E_F/\Delta = 2.5$, comparable to the measured value for $FeTe_{0.55}Se_{0.45}$ [11]. (c) Using a soft cantilever (Table S2 in [19]), the absolute change in MFM resonance frequency, $|\delta f|$, from the parity 1 state in a double flux quantum vortex is shown for both the continuum (red) and lattice (black) models and the low-temperature noise floor (horizontal dashed line) is calculated via Eq. 7. Note for this calculation the effective tip monopole is calculated for a nanowire on tip to be of strength $\tilde{m} \approx .3$ nAm, placed at an offset distance from the nanowire apex of $d = 4.4$ nm. Inset: Excess magnetic field gradient above the center of a double flux quantum vortex as a function of tip-sample separation $z$ above the sample surface, in the continuum (red) and lattice (black) models. This physical observable derived from the MZM wavefunction solution is then converted into an experimentally dependent resonance frequency shift $\delta f$ via Eq. 6 using the monopole-monopole approximation [19].

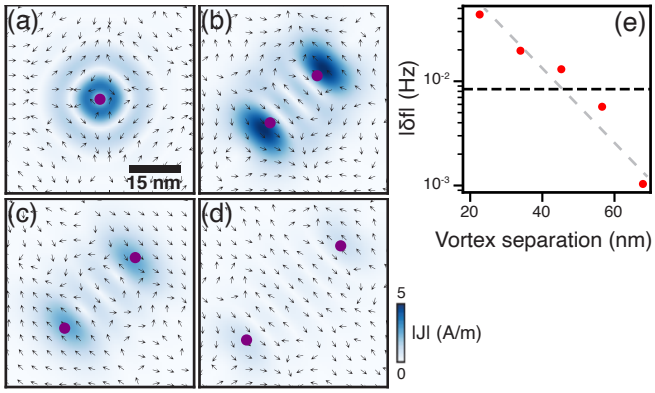


FIG. 3. Excess current density generated by overlap of two MZMs in the parity 1 state in the lattice model with $E_F/\Delta = 2.5$ for (a) the double flux quantum vortex and a vortex core separation of (b) $\sim 2\xi$, (c) $\sim 2.5\xi$, and (d) $\sim 3.5\xi$. As vortex cores, represented by purple dots, are separated, the current magnitude drops exponentially, leading to a drop in the excess resonance frequency shift of the MFM cantilever. (e) MFM cantilever resonance frequency shift as a function of vortex separation, calculated at a fixed height of 2 nm above the midpoint of the vortex pair. The diagonal gray dashed line is a guide to the eye showing exponential decay. The black dashed line shows the low-temperature noise floor (Eq. 7) calculated for a soft cantilever (Table S2 in [19]) with a nanowire on tip [32].

in Fig. 2(a-b). While the charge density will exert electrostatic forces on the MFM tip, screening by the background superconductor is expected to reduce this effect to a level undetectable by MFM outside of tip-sample separations in the tunneling regime where quasiparticle poisoning may dominate [29–31]. Therefore, we focus on the excess current density associated with $\Psi(r)$, given by the expectation value of the tangential component of the current operator,

$$j(r) = -ve\Psi^\dagger(r)\sigma_x\Psi(r). \tag{5}$$

The magnetic field gradient perpendicular to the surface $|dB_z/dz|$ generated by this current, shown in Fig. 2(c), is expected to be detectable by traditional Si cantilevers at tip-sample separation $\gtrsim 2$ nm where quasiparticle poisoning from tip-sample tunneling is not significant.

10 *Lattice Model - Two Vortices*—To analyze the magnetic signal generated by the more realistic case of two partially overlapping single flux quantum vortices, we numerically solved the Fu-Kane Hamiltonian (Eq. 1) on a lattice. The lattice realization breaks time-reversal symmetry on the lattice level (as expected from the fermion doubling theorem), but is parameterized to preserve the low-energy effective Hamiltonian consistent with Eq. 1. The result of the lattice model in the extreme limit of the double flux quantum vortex is shown in Fig. 2(c), demonstrating excellent agreement with the continuum model.

11 The Majorana signature can now also be studied with the spatial separation of vortices as a free input parameter. The current flow generated by the overlap of the two MZMs in the parity 1 state is shown in Fig. 3(a-d) for various spatial separations (the parity 0 case would have no such excess supercurrent). We calculate the change in resonance frequency of the MFM cantilever at a fixed height of 2 nm above the surface, as a function of the lateral separation between vortices, as shown in Fig. 3(e). The Majorana parity signal decays exponentially with vortex separation as expected, but the MZM overlap is still large enough to be detectable with vortex separations over 40 nm, several times $\xi \sim 12$ nm [11].

12 *MFM Sensitivity and Noise*—When the MFM tip approaches the vortex from above, the tip feels a force due to the magnetic field induced by the excess current density. Modeling the tip as a magnetic monopole, the cantilever frequency shifts in proportion to the magnetic field gradient with sensitivity

$$\delta f = \tilde{m}\frac{f_0}{2k}\frac{dB_z}{dz}, \tag{6}$$

where $k$ is the cantilever force constant, $f_0$ is the reso-

nance frequency, and $\widetilde{m}$ is an effective tip monopole. For typical Co coated pyramidal tips the effective monopole $\tilde{m}$ is expected to be $\sim 5$ times the hypothetical fundamental Dirac monopole $h/e\mu_0$, but $d$ is large $\sim 250$ nm from the tip apex [33], reducing the overall resonance frequency shift. In order to maximize the sensitivity of the measurement, it is optimal to use a Nd coated nanowire on tip [32] with a smaller effective monopole $\tilde{m} \sim 0.1\frac{h}{e\mu_0}$ and smaller offset $d \sim 4$ nm (Section IV in [19]). The *sensitivity* must be balanced against the three primary *noise* sources in frequency-modulated AFM: thermal, detector, and oscillator noise [34, 35] (Section IV in [19]). With optimized electronics and a typical silicon cantilever, even at low temperature the system will usually be dominated by thermal noise,

$$\delta f_{\text{therm}} = \sqrt{\frac{k_B T B f_0}{\pi k Q A^2}}, \tag{7}$$

where $B$ is the measurement bandwidth, $A$ is the oscillation amplitude, $Q$ is the quality factor, and $k_B$ is Boltzmann's constant. Then a stiffer cantilever lowers the noise floor as $\sqrt{f_0/k}$, but also reduces signal sensitivity as $f_0/k$, making softer cantilevers the optimal choice for a parity readout. A typical soft cantilever with $f_0 \sim 10$ kHz and $k \sim 0.01$ N/m is used to convert the calculated magnetic field gradient to a detectable frequency shift in Fig. 2(c). The corresponding noise floor for this cantilever, calculated in a 1 Hz bandwidth, is shown as a horizontal dashed line in Fig. 2(c) and Fig. 3(e). Other background signals from the conventional vortex supercurrent and tip stray magnetic field are constant across all vortices, as calculated in Section V of [19].

13 To read Majorana parity, we will need to bring two vortices together so their cores almost touch, overcoming the inter-vortex repulsion. In $FeTe_{0.55}Se_{0.45}$, which is at the extreme type-II limit, the vortex-vortex repulsion approaches 10 pN for a 100 nm thick film as the separation approaches $2\xi$ [36] (Section VI in [19]). Therefore, we must strongly pin one vortex in a region where topological band inversion guarantees a surface MZM [37], while we bring another vortex towards it. Though pinning forces in clean bulk FeSe can be on the order of fN [38], a promising measurement in ion-irradiated $FeTe_{0.55}Se_{0.45}$ showed that some vortices can be fixed by collective pinning in relatively clean areas, avoiding MZM burial or poisoning by normal quasiparticles present at the pinning site, and leaving a sharp zero bias conductance peak (ZBCP) intact on the surface [39].

14 *Parity Lifetime Measurement*—Despite its topological nature, the Majorana pair has a finite parity lifetime due to interactions between the Majoranas and stray quasiparticles that cause decoherence known as quasiparticle poisoning [40]. Quasiparticle poisoning leads to a fluctuation of the occupation of the lowest-energy vortex bound state, which is associated with the excess magnetic field we propose as a parity readout signal. These discrete flips in the Majorana parity between 0 and 1 would thus give rise to telegraph noise in the force on the MFM tip as it is held above the vortex cores. Other commonly-observed telegraph noise in superconducting devices arises from cosmic rays [41], fluctuating charges [42] or spins [43] in the adjacent oxide tunnel junction, or surface hydrogen or oxygen adsorbents [44, 45]. These mechanisms are infrequent or inapplicable to the UHV-cleaved bulk $FeTe_{0.55}Se_{0.45}$ sample proposed here. Nematic [46, 47] or magnetic [48] domain switching in bulk materials can likely be ruled out due to domain freezing at low temperature. Nonlinear $1/f$ noise has been observed only *above* $T_c$ in Fe(Te,Se) films, and attributed to voltage-driven or thermally-activated interband coupling [49]. Therefore, observation of telegraph noise in UHV-cleaved $FeTe_{0.55}Se_{0.45}$ deep in the superconducting state at zero bias and mK temperature, would suggest that the fluctuation is indeed Majorana in nature.

15 Majorana telegraph noise should be measurable if the quasiparticle poisoning is slower than the acquisition of the force measurement. The characteristic rate of telegraph noise would yield an estimate of the quasiparticle poisoning timescale that limits the qubit lifetime, which has been difficult to model and poorly understood. To minimize quasiparticle poisoning, the tip must be out of tunneling range, $z \gtrsim 2$ nm from the surface. From Fig. 2(c), this $z$ corresponds to an expected signal $\delta f \sim .01$ Hz, which requires a measurement time $\sim 100$ s in frequency-modulated MFM. Using amplitude-modulated MFM, the measurement duration is limited by the response time of the cantilever to a changing force. Lossy qPlus cantilevers with $Q \sim 100$ and $f_0 \sim 10$ kHz could enable measurement duration $Q/f_0 \sim 10$ ms.

16 *Conclusion*—We have presented a scheme for the pinning, dragging, parity readout, and lifetime of a pair of MZMs in the vortex cores of topological superconductors using MFM. We have shown that MFM cantilevers can be sensitive enough to measure the change in supercurrent when the resulting fermionic state is occupied, even when the two vortex cores are not completely overlapping. While we have explicitly demonstrated numerical feasibility only for $FeTe_{0.55}Se_{0.45}$, we expect the same methodology will be applicable to other topological superconductors that realize the Fu-Kane model on the surface, including stoichiometric materials with uniform chemical potential (Table S1 in [19]). Thus, we have laid out a novel pathway toward the experimental realization of topologically protected quantum logic.

This work is supported by the U.S. National Science Foundation Grant No. OMA-1936246.

* jaydsau@umd.edu

† jhoffman@physics.harvard.edu


[1] A. Kitaev, Fault-tolerant quantum computation by anyons, Annals of Physics **303**, 2 (2003).

[2] S. Das Sarma, M. Freedman, and C. Nayak, Majorana zero modes and topological quantum computation, npj Quantum Information **1**, 15001 (2015).

[3] A. R. Akhmerov, Topological quantum computation away from the ground state using Majorana fermions, Physical Review B **82**, 020509 (2010).

[4] H. Røising, R. Ilan, T. Meng, S. Simon, and F. Flicker, Finite temperature effects on Majorana bound states in chiral $p$-wave superconductors, SciPost Physics **6**, 055 (2019).

[5] S. M. Albrecht, A. P. Higginbotham, M. Madsen, F. Kuemmeth, T. S. Jespersen, J. Nygård, P. Krogstrup, and C. M. Marcus, Exponential protection of zero modes in Majorana islands, Nature **531**, 206 (2016).

[6] H. J. Suominen, M. Kjaergaard, A. R. Hamilton, J. Shabani, C. J. Palmstrøm, C. M. Marcus, and F. Nichele, Zero-Energy Modes from Coalescing Andreev States in a Two-Dimensional Semiconductor-Superconductor Hybrid Platform, Physical Review Letters **119**, 176805 (2017).

[7] L. Fu and C. L. Kane, Superconducting Proximity Effect and Majorana Fermions at the Surface of a Topological Insulator, Physical Review Letters **100**, 096407 (2008).

[8] N. Read and D. Green, Paired states of fermions in two dimensions with breaking of parity and time-reversal symmetries and the fractional quantum Hall effect, Physical Review B **61**, 10267 (2000).

[9] N. Hao and J. Hu, Topological quantum states of matter in iron-based superconductors: from concept to material realization, National Science Review **6**, 213 (2019).

[10] E. J. König and P. Coleman, Crystalline-Symmetry-Protected Helical Majorana Modes in the Iron Pnictides, Physical Review Letters **122**, 207001 (2019).

[11] D. Wang, L. Kong, P. Fan, H. Chen, S. Zhu, W. Liu, L. Cao, Y. Sun, S. Du, J. Schneeloch, R. Zhong, G. Gu, L. Fu, H. Ding, and H. J. Gao, Evidence for Majorana bound states in an iron-based superconductor, Science **362**, 333 (2018).

[12] T. Machida, Y. Sun, S. Pyon, S. Takeda, Y. Kohsaka, T. Hanaguri, T. Sasagawa, and T. Tamegai, Zero-energy vortex bound state in the superconducting topological surface state of Fe(Se,Te), Nature Materials **18**, 811 (2019).

[13] L. Kong, S. Zhu, M. Papaj, H. Chen, L. Cao, H. Isobe, Y. Xing, W. Liu, D. Wang, P. Fan, Y. Sun, S. Du, J. Schneeloch, R. Zhong, G. Gu, L. Fu, H.-J. Gao, and H. Ding, Half-integer level shift of vortex bound states in an iron-based superconductor, Nature Physics **15**, 1181 (2019).

[14] S. Zhu, L. Kong, L. Cao, H. Chen, M. Papaj, S. Du, Y. Xing, W. Liu, D. Wang, C. Shen, F. Yang, J. Schneeloch, R. Zhong, G. Gu, L. Fu, Y.-Y. Zhang, H. Ding, and H.-J. Gao, Nearly quantized conductance plateau of vortex zero mode in an iron-based superconductor, Science **367**, 189 (2020).

[15] Q. Liu, C. Chen, T. Zhang, R. Peng, Y.-J. Yan, C.-H.-P. Wen, X. Lou, Y.-L. Huang, J.-P. Tian, X.-L. Dong, G.-W. Wang, W.-C. Bao, Q.-H. Wang, Z.-P. Yin, Z.-X. Zhao, and D.-L. Feng, Robust and Clean Majorana Zero Mode in the Vortex Core of High-Temperature Superconductor $(Li_{0.84}Fe_{0.16})OHFeSe$, Physical Review X **8**, 041056 (2018).

[16] W. Liu, L. Cao, S. Zhu, L. Kong, G. Wang, M. Papaj, P. Zhang, Y.-B. Liu, H. Chen, G. Li, F. Yang, T. Kondo, S. Du, G.-H. Cao, S. Shin, L. Fu, Z. Yin, H.-J. Gao, and H. Ding, A new Majorana platform in an Fe-As bilayer superconductor, Nature Communications **11**, 5688 (2020).

[17] L. Kong, L. Cao, S. Zhu, M. Papaj, G. Dai, G. Li, P. Fan, W. Liu, F. Yang, X. Wang, S. Du, C. Jin, L. Fu, H.-J. Gao, and H. Ding, Majorana zero modes in impurity-assisted vortex of LiFeAs superconductor, Nature Communications **12**, 4146 (2021).

[18] C. Caroli, P. G. de Gennes, and J. Matricon, Bound fermion states on a vortex line in a type II superconducor, Physics Letters **9**, 307 (1964).

[19] See Supplemental Material at [URL will be inserted by publisher] for a table of Fe-based superconductors exhibiting MZMs; additional theoretical details including the derivation and solution of the radial BdG equation and the chiral limit; and additional experimental details including MFM sensitivity and noise floor, the circulating supercurrent, stray magnetic fields, and pinning forces associated with conventional vortices.

[20] A. Kremen, S. Wissberg, N. Haham, E. Persky, Y. Frenkel, and B. Kalisky, Mechanical Control of Individual Superconducting Vortices, Nano Letters **16**, 1626 (2016).

[21] J.-Y. Ge, V. N. Gladilin, J. Tempere, C. Xue, J. T. Devreese, J. Van de Vondel, Y. Zhou, and V. V. Moshchalkov, Nanoscale assembly of superconducting vortices with scanning tunnelling microscope tip, Nature Communications **7**, 13880 (2016).

[22] B. W. Gardner, J. C. Wynn, D. A. Bonn, R. Liang, W. N. Hardy, J. R. Kirtley, V. G. Kogan, and K. A. Moler, Manipulation of single vortices in $YBa_2Cu_3O_{6.354}$ with a locally applied magnetic field, Applied Physics Letters **80**, 1010 (2002).

[23] P. Zhang, K. Yaji, T. Hashimoto, Y. Ota, T. Kondo, K. Okazaki, Z. Wang, J. Wen, G. D. Gu, H. Ding, and S. Shin, Observation of topological superconductivity on the surface of an iron-based superconductor, Science **360**, 182 (2018).

[24] T. Hanaguri, S. Niitaka, K. Kuroki, and H. Takagi, Unconventional $s$-Wave Superconductivity in Fe(Se,Te), Science **328**, 474 (2010).

[25] J.-X. Yin, Z. Wu, J.-H. Wang, Z.-Y. Ye, J. Gong, X.-Y. Hou, L. Shan, A. Li, X.-J. Liang, X.-X. Wu, J. Li, C.-S. Ting, Z.-Q. Wang, J.-P. Hu, P.-H. Hor, H. Ding, and S. H. Pan, Observation of a robust zero-energy bound state in iron-based superconductor Fe(Te,Se), Nature Physics **11**, 543 (2015).

[26] H. Lohani, T. Hazra, A. Ribak, Y. Nitzav, H. Fu, B. Yan, M. Randeria, and A. Kanigel, Band inversion and topology of the bulk electronic structure in $FeSe_{0.45}Te_{0.55}$, Physical Review B **101**, 245146 (2020).

[27] H. Nielsen and M. Ninomiya, The Adler-Bell-Jackiw anomaly and Weyl fermions in a crystal, Physics Letters B **130**, 389 (1983).

[28] R. Jackiw and P. Rossi, Zero modes of the vortex-fermion system, Nuclear Physics B **190**, 681 (1981).

[29] S. Das Sarma, C. Nayak, and S. Tewari, Proposal to stabilize and detect half-quantum vortices in strontium ruthenate thin films: Non-abelian braiding statistics of vortices in a $p_x + ip_y$ superconductor, Physical Review B

**73**, 220502 (2006).

[30] C.-H. Lin, J. D. Sau, and S. Das Sarma, Zero-bias conductance peak in Majorana wires made of semiconductor/superconductor hybrid structures, Physical Review B **86**, 224511 (2012).

[31] G. Ben-Shach, A. Haim, I. Appelbaum, Y. Oreg, A. Yacoby, and B. I. Halperin, Detecting Majorana modes in one-dimensional wires by charge sensing, Physical Review B **91**, 045403 (2015).

[32] Z. Deng, E. Yenilmez, J. Leu, J. E. Hoffman, E. W. J. Straver, H. Dai, and K. A. Moler, Metal-coated carbon nanotube tips for magnetic force microscopy, Applied Physics Letters **85**, 6263 (2004).

[33] E. W. J. Straver, J. E. Hoffman, O. M. Auslaender, D. Rugar, and K. A. Moler, Controlled manipulation of individual vortices in a superconductor, Applied Physics Letters **93**, 172514 (2008).

[34] T. R. Albrecht, P. Grütter, D. Horne, and D. Rugar, Frequency modulation detection using high-Q cantilevers for enhanced force microscope sensitivity, Journal of Applied Physics **69**, 668 (1991).

[35] J. Schwenk, S. Kim, J. Berwanger, F. Ghahari, D. Walkup, M. R. Slot, S. T. Le, W. G. Cullen, S. R. Blankenship, S. Vranjkovic, H. J. Hug, Y. Kuk, F. J. Giessibl, and J. A. Stroscio, Achieving $\mu$eV tunneling resolution in an in-operando scanning tunneling microscopy, atomic force microscopy, and magnetotransport system for quantum materials research, Review of Scientific Instruments **91**, 071101 (2020).

[36] A. Chaves, F. M. Peeters, G. A. Farias, and M. V. Milošević, Vortex-vortex interaction in bulk superconductors: Ginzburg-Landau theory, Physical Review B **83**, 054516 (2011).

[37] T. Barik and J. D. Sau, Signatures of nontopological patches on the surface of topological insulators, Physical Review B **105**, 035128 (2022).

[38] I. P. Zhang, J. C. Palmstrom, H. Noad, L. Bishop-Van Horn, Y. Iguchi, Z. Cui, E. Mueller, J. R. Kirtley, I. R. Fisher, and K. A. Moler, Imaging anisotropic vortex dynamics in FeSe, Physical Review B **100**, 024514 (2019).

[39] F. Massee, P. O. Sprau, Y.-L. Wang, J. C. S. Davis, G. Ghigo, G. D. Gu, and W.-K. Kwok, Imaging atomic-scale effects of high-energy ion irradiation on superconductivity and vortex pinning in Fe(Se,Te), Science Advances **1**, e1500033 (2015).

[40] G. Catelani, J. Koch, L. Frunzio, R. J. Schoelkopf, M. H. Devoret, and L. I. Glazman, Quasiparticle Relaxation of Superconducting Qubits in the Presence of Flux, Physical Review Letters **106**, 077002 (2011).

[41] A. P. Vepsäläinen, A. H. Karamlou, J. L. Orrell, A. S. Dogra, B. Loer, F. Vasconcelos, D. K. Kim, A. J. Melville, B. M. Niedzielski, J. L. Yoder, S. Gustavsson, J. A. Formaggio, B. A. VanDevender, and W. D. Oliver, Impact of ionizing radiation on superconducting qubit coherence, Nature **584**, 551 (2020).

[42] J. M. Martinis, K. B. Cooper, R. McDermott, M. Steffen, M. Ansmann, K. D. Osborn, K. Cicak, S. Oh, D. P. Pappas, R. W. Simmonds, and C. C. Yu, Decoherence in Josephson Qubits from Dielectric Loss, Physical Review Letters **95**, 210503 (2005).

[43] S. Sendelbach, D. Hover, A. Kittel, M. Mück, J. M. Martinis, and R. McDermott, Magnetism in SQUIDs at Millikelvin Temperatures, Physical Review Letters **100**, 227006 (2008).

[44] P. Kumar, S. Sendelbach, M. A. Beck, J. W. Freeland, Z. Wang, H. Wang, C. C. Yu, R. Q. Wu, D. P. Pappas, and R. McDermott, Origin and Reduction of $1/f$ Magnetic Flux Noise in Superconducting Devices, Physical Review Applied **6**, 041001 (2016).

[45] S. E. d. Graaf, L. Faoro, J. Burnett, A. A. Adamyan, A. Y. Tzalenchuk, S. E. Kubatkin, T. Lindström, and A. V. Danilov, Suppression of low-frequency charge noise in superconducting resonators by surface spin desorption, Nature Communications **9**, 1143 (2018).

[46] D. S. Caplan, V. Orlyanchik, M. B. Weissman, D. J. Van Harlingen, E. H. Fradkin, M. J. Hinton, and T. R. Lemberger, Anomalous Noise in the Pseudogap Regime of $YBa_2Cu_3O_{7-\delta}$, Physical Review Letters **104**, 177001 (2010).

[47] E. W. Carlson, K. A. Dahmen, E. Fradkin, and S. A. Kivelson, Hysteresis and Noise from Electronic Nematicity in High-Temperature Superconductors, Physical Review Letters **96**, 097003 (2006).

[48] M. Fischer, M. T. Elm, H. Kato, S. Sakita, S. Hara, and P. J. Klar, Analysis of magnetic random telegraph noise in individual arrangements of a small number of coupled MnAs nanoclusters, Physical Review B **92**, 165306 (2015).

[49] C. Barone, E. Bellingeri, M. Adamo, E. Sarnelli, C. Ferdeghini, and S. Pagano, Electric field activated nonlinear $1/f$ fluctuations in Fe(Te, Se) superconductors, Superconductor Science and Technology **26**, 075006 (2013).

# Supplemental material for Scheme for Majorana Manipulation Using Magnetic Force Microscopy

Benjamin H. November,[1] Jay D. Sau,[2] James R. Williams,[3] and Jennifer E. Hoffman[1,4]

[1] *Department of Physics, Harvard University, Cambridge, Massachusetts 02138, USA*

[2] *Condensed Matter Theory Center and Joint Quantum Institute, Department of Physics, University of Maryland, College Park, Maryland 20742, USA*

[3] *Joint Quantum institute, Center for Nanophysics and Advanced Materials, Department of Physics, University of Maryland, College Park, Maryland 20742, USA*

[4] *School of Engineering & Applied Sciences, Harvard University, Cambridge, Massachusetts 02138, USA*

(Dated: June 14, 2023)

## I. MATERIALS HOSTING MAJORANA ZERO MODES IN VORTEX CORES

**S1** Zero bias conductance peaks (ZBCPs) suggestive of Majorana zero modes (MZMs) have been observed in the vortex cores of several Fe-based superconductors. It remains crucial to distinguish the ZBCP from the conventional Caroli-deGennes-Matricon (CdGM) subgap states of the vortex, which scale as $\pm\mu\Delta^2/E_F$ [1], where $\Delta$ is the superconducting gap, $E_F$ is the chemical potential, and $\mu = \frac{1}{2}, \frac{3}{2}, \frac{5}{2}, ...$ in a conventional vortex or $\mu = 1, 2, 3, ...$ in a vortex with MZM [2, 3]. Table S1 shows that MZMs can be distinguished from CdGM states in several Fe-based superconductors by scanning tunneling microscopy (STM).

**S2** The spectral energy resolution of scanning tunneling microscopy (STM) is thermally limited by the convolution of the tip and sample Fermi function to approximately $3.5k_BT$. Thus for a dilution fridge STM with base electron temperature $\sim 40$ mK (see Fig. 6 in Ref. [4]), the energy resolution is as good as $\sim 12$ $\mu$eV. This resolution is more than an order of magnitude smaller than the smallest reported gap between the ZBCP and the lowest CdGM states, allowing for the experimental observation of isolated ZBCPs in vortex cores.

| **Experiment** | **Operating Temp.** | **Material** | **SC Gap** ($\Delta$) | **Fermi Level** ($E_F$) | **Lowest Observed CdGM (no ZBCP)** | **Lowest Observed CdGM (with ZBCP)** |
|---|---|---|---|---|---|---|
| M. Chen, Nat Com (2018) [5] | $\sim 400$ mK | $FeTe_{0.55}Se_{0.45}$ | 1.1 meV | $\sim 4$ meV | 0.45 meV | – |
| D. Wang, Science (2018) [6] | $\sim 550$ mK | $FeTe_{0.55}Se_{0.45}$ | 1.8 meV | 4.4 meV | 0.34 meV | 0.68 meV |
| T. Machida, Nat Mat (2019) [7] | $T_{el} \sim 85$ mK | $FeTe_{0.55}Se_{0.45}$ | 1.5 meV | 10 meV | 0.10 meV | 0.17 meV |
| L. Kong, Nat Phys (2019) [8] | $\sim 550$ mK | $FeTe_{0.55}Se_{0.45}$ | 2.2 meV | 2.6 meV | 0.26 meV | 0.65 meV |
| S. Zhu, Science (2020) [9] | $T_{el} \sim 377$ mK | $FeTe_{0.55}Se_{0.45}$ | 1.1 meV | | 0.13 meV | 0.31 meV |
| C. Chen, PRL (2020) [10] | $T_{el} \sim 1.18$ K | $FeSe/SrTiO_3$ | 10.6 meV | 60 meV | 0.54 meV | – |
| Q. Liu, PRX (2018) [11] | $\sim 400$ mK | $(Li_{0.84}Fe_{0.16})OHFeSe$ | 5.7 meV | 57 meV | – | 0.77 meV |
| W. Liu, Nat Com (2020) [12] | $T_{el} \sim 690$ mK | $CaKFe_4As_4$ | 5.8 meV | 20.9 meV | – | 1.2 meV |
| L. Kong, Nat Com (2021) [13] | $\sim 400$ mK | LiFeAs | 2.1 meV | 4.0 meV | 0.4 meV | 0.9 meV |
| X. Chen, PRL (2021) [14] | $\sim 400$ mK | $KCa_2Fe_4As_4F_2$ | 4.3 meV | 24 meV | 0.8 meV | – |

TABLE S1. Previous STM experiments on vortices in $FeTe_{0.55}Se_{0.45}$ and other Fe-based superconductors.

## II. DERIVATION AND SOLUTION OF RADIAL BDG EQUATION

**S3** We begin by recalling the BdG Hamiltonian in polar coordinates,

$$\begin{aligned} H = &[-iv\{(\sigma_x \cos\theta + \sigma_y \sin\theta)\partial_r + \frac{1}{r}(\sigma_y \cos\theta - \sigma_x \sin\theta)\partial_\theta\}]\tau_z \\ &- E_F\tau_z + \Delta(r)\{\cos n\theta\tau_x + \sin n\theta\tau_y\}. \end{aligned} \tag{S1}$$

We note that it commutes with the total angular momentum operator

$$J = L + \frac{1}{2}(\sigma_z + n\tau_z), \tag{S2}$$

where $L = -i\partial_\theta$ is the orbital angular momentum operator. This allows us to focus on solutions with eigenvalues $J = m$. The spectrum of excitations of this system is found by solving the eigenvalue problem

$$H\Psi_m(r,\theta) = E\Psi_m(r,\theta). \tag{S3}$$

The angular dependence for such states is written as

$$\begin{aligned}\Psi_m(r,\theta') &= e^{i\theta' L}\Psi_m(r,\theta)|_{\theta=0} \\ &= e^{-i\theta'(\sigma_z+n\tau_z-2m)/2}\Psi_m(r,0).\end{aligned} \tag{S4}$$

Applying this transformation, we can isolate the $\theta$ dependence of the BdG equation as

$$e^{\frac{i\theta}{2}(\sigma_z+n\tau_z-2m)}He^{-\frac{i\theta}{2}(\sigma_z+n\tau_z-2m)}\Psi_m(r,0) = E\Psi_m(r,0), \tag{S5}$$

where

$$\begin{aligned}H_m &= e^{\frac{i\theta}{2}(\sigma_z+n\tau_z-2m)}He^{-\frac{i\theta}{2}(\sigma_z+n\tau_z-2m)} \\ &= -iv\sigma_x\tau_z\partial_r - \tau_z[E_F - \frac{i}{r}\sigma_y\frac{i}{2}(\sigma_z+n\tau_z-2m)] \\ &+ \Delta(r)\tau_x.\end{aligned} \tag{S6}$$

The 1-D radial BdG equation then takes the form

$$\begin{aligned}&[-iv\sigma_x\tau_z\partial_r + \tau_z\{-E_F + \frac{i}{r}\sigma_y(i/2)(\sigma_z+n\tau_z-2m)\} \\ &+ \Delta(r)\tau_x - E]\Psi(r) = 0.\end{aligned} \tag{S7}$$

We then set $v = \Delta_0 = 1$ and make the rotation $\sigma_x \to \sigma_y$ to find

$$\begin{aligned}&[\partial_r + \{-iE_F\sigma_y + \frac{1}{2r}(1+\sigma_z(n\tau_z-2m))\} \\ &- \tanh(r)\tau_y\sigma_y - iE\sigma_y\tau_z]\Psi(r) = 0.\end{aligned} \tag{S8}$$

**S4** Eq. S8 can in principle be solved as an initial value problem from $r = 0$ to $r = \infty$. In the limit $r \to 0$, the $\frac{1}{r}$ term dominates and thus the initial value $\Psi(r \to 0)$ must satisfy the constraint

$$\{1 + \sigma_z(n\tau_z - 2m)\}\Psi(r \to 0) = \alpha\Psi(r \to 0), \tag{S9}$$

where $\alpha \leq 0$. Let us now focus on the $m = \frac{1}{2}$ angular momentum channel of a double vortex ($n = 2$). The initial condition then satisfies

$$(1 - \sigma_z + 2\sigma_z\tau_z)\Psi(r \to 0) = \alpha\Psi(r \to 0). \tag{S10}$$

This allows initial conditions $\Psi_j(r \to 0) = \Psi_j$ where $\Psi_{j=1,2}$ are the two orthonormal vectors with $\sigma_z\tau_z = -1$. Let us represent the solutions to the initial value problem defined by Eq. S8 as $\Psi_j(r)$. A general solution matching the boundary conditions as $r \to 0$ is given by

$$\Psi(r) = \sum_j c_j\Psi_j(r). \tag{S11}$$

**S5** Next we consider the boundary conditions at $r \to \infty$, where Eq. S8 takes the form

$$[\partial_r - iE_F\sigma_y - \tau_y\sigma_y - iE\sigma_y\tau_z]\Psi = 0. \tag{S12}$$

In this limit $\Psi(r) = \Psi e^{-zr}$ where convergent solutions require $Re[z] > 0$. Substituting, we get

$$[-iE_F\sigma_y - \tau_y\sigma_y - iE\sigma_y\tau_z]\Psi = z\Psi. \tag{S13}$$

Let us denote the two eigenvectors with the convergent eigenvalues as $\tilde{\Psi}_{j=1,2}$. We can then define $\tilde{\Psi}_j(r)$ to be the solutions of Eq. S8 with boundary conditions $\tilde{\Psi}_j(r \to \infty) = \tilde{\Psi}_j e^{-z_j r}$. A general solution matching the boundary conditions as $r \to \infty$ is given by

$$\Psi(r) = \sum_j \tilde{c}_j \tilde{\Psi}_j(r). \tag{S14}$$

S6 For a complete solution, the two solutions at small and large $r$, given by Eq. S11 and Eq. S14, respectively, must match at an intermediate $r = R$. Since this is a linear condition for 4 component wave-functions with 4 coefficients, such a matching is possible only if the energy $E$ satisfies the condition

$$M(E) = \begin{bmatrix}\Psi_1(R) & \Psi_2(R) & \tilde{\Psi}_1(R) & \tilde{\Psi}_2(R)\end{bmatrix} = 0. \tag{S15}$$

Since Eq. S8 is real, $M(E)$ is real and the solutions can be determined by simple root finding. The null vector of the matrix provides us with the coefficients of $c_j$, which then allows us to construct $\Psi(r)$ using Eq. S11. In practice we can compute $\tilde{\Psi}_j(R)$ by solving Eq. S8 in reverse from some large $R' \gg R$ with an arbitrary initial condition. While the resulting solution contains the states with $Re[z] < 0$, the amplitudes of such states are exponentially small. It can be shown that this is equivalent to considering $\Psi_j(R')$ and setting the projector to zero. Therefore, for practical purposes we solve the simpler problem

$$M_1(E) = \begin{bmatrix}(1 + \sigma_z\tau_z)\,\Psi_1(R') & \Psi_2(R')\end{bmatrix} = 0. \tag{S16}$$

As before, the bound state energy is the root in $E$ for which the above matrix has a zero eigenvalue. The null vector of the matrix provides us with the coefficients of $c_j$, which then allows us to construct $\Psi(r)$ using Eq. S11.

## III. THE CHIRAL LIMIT

S7 The radial equation for the vortex (Eq. S8) is analytically solvable in the chiral limit i.e. $E_F = 0$ and $m = \frac{1}{2}$, in which case there is a solution for $E = 0$. In this limit Eq. S8 becomes

$$[-\partial_r - \frac{1}{r}(n\sigma_z\tau_z)/2 + \tanh(r)\tau_y\sigma_x]\Psi(r) = 0. \tag{S17}$$

This equation is easy to solve since the comprising matrices $(1, \sigma_z\tau_z$ and $\tau_y\sigma_x)$ commute. The solution to these equations are then formally written as

$$\Psi(r) = r^{-(n\sigma_z\tau_z)/2}\cosh(r)^{\tau_y\sigma_x}\Psi_0. \tag{S18}$$

For a double vortex this leads to a unique solution of the form

$$\Psi(r) = Nr\mathrm{sech}(r)\Psi_0, \tag{S19}$$

where $\Psi_0$ is defined by the equation $\sigma_z\tau_z\Psi_0 = \tau_y\sigma_x\Psi_0 = -\Psi_0$ and $N$ is a normalization constant. Adding a finite chemical potential $E_F$ doesn't affect the wave-function much at lowest order in perturbation theory, but shifts the energy to

$$E \simeq -E_F\Psi_0^\dagger\tau_z\Psi_0 = 0. \tag{S20}$$

The current density would be given by

$$j(r) = vN^2r^2\mathrm{sech}^2(r)\Psi_0^\dagger\sigma_y\Psi_0 = 0. \tag{S21}$$

This means one needs to consider the wave-function contribution of order $E_F$, which is out of the scope of our arguments.

## IV. AFM SENSITIVITY

S8 The horizontal dashed lines representing the MFM noise floors in Fig. 2(c) and Fig. 3(e) are calculated taking into account typical measurement noise contributions. Frequency-modulated AFM detects a force gradient due to the tip-sample interaction through a shift in the resonance frequency of the cantilever from $f_0$ to $f_0 + \delta f$. There are three main sources of noise to consider in frequency-modulated AFM: thermal noise $\delta f_{\text{therm}}$, detector noise $\delta f_{\text{det}}$, and oscillator noise $\delta f_{\text{osc}}$, given by Refs. [15, 16] as

$$\delta f_{\text{therm}} = \sqrt{\frac{k_B T B f_0}{\pi k Q A^2}} \tag{S22}$$

$$\delta f_{\text{det}} = \sqrt{\frac{2}{3}} \frac{n B^{3/2}}{A} \tag{S23}$$

$$\delta f_{\text{osc}} = \frac{f_0 n}{\sqrt{2} A Q} \sqrt{B} \tag{S24}$$

$$\delta f_{\text{total}} = \sqrt{\delta f_{\text{therm}}^2 + \delta f_{\text{det}}^2 + \delta f_{\text{osc}}^2} \tag{S25}$$

where $k$ is the cantilever stiffness, $n$ is the deflection noise density, $B$ is the measurement bandwidth, $A$ is the oscillation amplitude, $Q$ is the quality factor, and $k_B$ is Boltzmann's constant. With optimized electronics and a typical silicon cantilever, the thermal noise contribution will dominate, even at low temperature. Table S2 gives examples of both stiff and soft NANOSENSORS$^{\text{TM}}$ cantilevers and the resulting baseline noise level ($\delta f_{\text{total}}$) that can be expected with reasonable operating conditions ($T = 40$ mK, $A \sim 500$ pm, $B \sim 1$ Hz, and $n \sim 150$ fm/$\sqrt{\text{Hz}}$). Higher $k$ provided by the stiffer cantilever lowers the thermal noise floor as $\sim \sqrt{f_0/k}$, but also reduces sensitivity to the parity 1 signal as $\sim f_0/k$, making softer cantilevers the optimal choice for a parity readout.

| | NANOSENSORS$^{\text{TM}}$ part number | $f_0$ (kHz) | $k$ (N/m) | $Q$ | Noise Floor $\delta f_{\text{total}}$ (mHz) | Optimal use |
|---|---|---|---|---|---|---|
| Stiff | SSS-MFMR [17] | 75 | 2.8 | 30,000 | 1.0 | Vortex manipulation |
| Soft | QP-SCONT [18] | 10 | 0.01 | 10,000 | 8.4 | Parity readout |
| Very Soft | Custom ion-etched [19, 20] | 5.5 | $1.1 \times 10^{-4}$ | 30,000 | 1.1 | Parity readout |

TABLE S2. Commercially-available mechanical cantilevers for different aspects of Majorana manipulation and readout.

S9 Although softer cantilevers are more sensitive to the parity readout, they are also more prone to snapping to the surface at the reduced tip-sample separations necessary to perform tunneling measurements of the ZBCP. A soft pendulum-style cantilever could be used to prevent snap-in, at the expense of lateral spatial resolution and vortex manipulation force [21], as shown in Figure S1 (a). One such very soft cantilever which greatly increases force resolution is listed in Table S2. Since the change in resonance frequency scales inversely with the stiffness, $k$, a softer cantilever is ideal for the readout of the parity of the MZM pairs. While this would normally also increase the thermal noise as $k^{-\frac{1}{2}}$, the larger oscillation amplitude, $A$, in the vertical orientation can make the detectable force noise floor even lower compared to the traditional horizontal case. Using the cantilever parameters for the custom ion-etched very soft cantilever [19, 20] with an oscillation amplitude of $A = 16$ nm gives a noise floor as low as $\delta f_{\text{total}} \sim 1$ mHz, with a higher response signal compared to the horizontal cantilever measurements, as shown in Figure S1 (b,c).

In addition to the cantilever, the type of tip itself is also important in the measured MFM response to the parity 1 signal. The geometry as well as the thickness and material choice for the magnetic coating will change the stray

| | tip geometry | coating material | thickness (nm) | $d$ (nm) | $\tilde{m}$ (nAm) |
|---|---|---|---|---|---|
| 1 | SSS-MFMR pyramid [17] | NdFeB | 1 | 5.5 | 0.28 |
| 2 | 250 nm nanotube [22] | NdFeB | 6 | 4.4 | 0.32 |
| 3 | Veeco MESP [23] | CoCr (Veeco-proprietary) | – | $\sim 250$ | 18 |
| 4 | Auslaender pyramid [24] | Fe | 60 | $\sim 350$ | $\sim 30$ |

TABLE S3. Effective $\tilde{m}$ and $d$ in the monopole approximation of various cantilever tips considered for this experiment (1,2) or used previously in literature (3,4). The specific values for rows 1-2 are dependent on the exact geometry of the tip as well as the magnetic coating material and thickness.

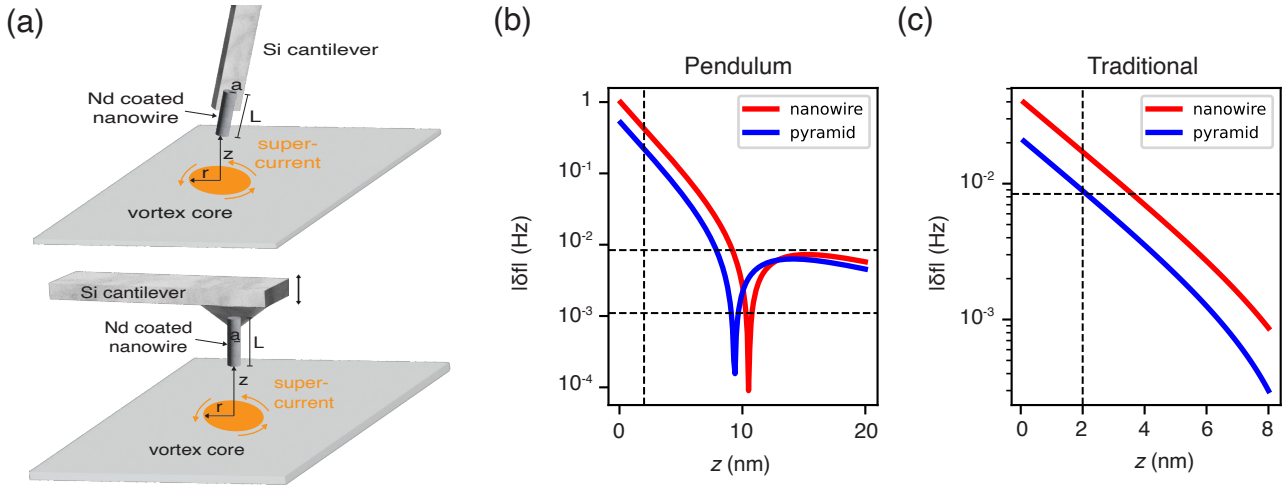


FIG. S1. (a) Conceptual diagram of the MFM cantilever in the vertical pendulum (top) and traditional horizontal (bottom) geometry with a Nd coated carbon nanotube tip. Dimensions of the nanowire are exaggerated compared to the macroscopic tip. Calculated stray magnetic field of both the Nd coated nanowire (red) and pyramid (blue) from the analytical model given by Eqn. S39 as a function of height above the sample surface in the (b) pendulum and (c) traditional horizontal geometries. The stray field is calculated where it is the largest on the surface before the Meissner screening, for the point directly beneath the tip, here set as the origin. Horizontal black dashed lines show the estimated MFM noise floor in the horizontal geometry of $\sim 8$ mHz and pendulum geometry of $\sim 1$ mHz. Vertical black dashed line shows the tunneling limit tip-sample separation of $\sim 2$ nm.

field, and therefore play a role in the sensitivity of the measurement. These specifics of the tip can be simplified in the monopole approximation as the effective monopole strength $\tilde{m}$ and offset $d$. We can model the tip as an extended object with a magnetic coating of thickness $t$ and remnant magnetization $M_r$. The stray field can then be calculated via

$$\vec{B} = \frac{\mu_0}{4\pi} \int_V \frac{3(\vec{M}_r \cdot (\hat{r} - \hat{r'}))(\hat{r} - \hat{r'}) - \vec{M}_r}{(r - r')^3} d\tau' \tag{S26}$$

where $\vec{r'}$ is the vector pointing to each differential volume element within the magnetic layer of the tip and $\vec{r}$ is the point where the field is evaluated at.

With a tip geometry and magnetic coating given, the calculated stray field perpendicular to the surface can then be fit to the equivalent field of an effective magnetic monopole given by

$$B_z^{\text{mono}} = \mu_0 \tilde{m} \frac{z + d}{(r^2 + (z + d)^2)^{3/2}}. \tag{S27}$$

With these effective monopole parameters, we can then calculate the expected MFM change in resonance frequency via Eqn. 6 of the main text. The effective monopole parameters for two types of tip geometries have been calculated in Table S3 rows 1,2: a pyramidal tip coated with 1 nm and a carbon nanotube coated with 6 nm of NdFeB, respectively, on a non-magnetized larger Si cantilever. The pyramid was found to give the highest signal response with a base of 50 $\mu$m and a height of 5 $\mu$m, well within reason of commercial cantilever fabrication, while the nanowire (modelled as a solid cylinder of magnetic material) should be made as long as possible to maximise the parity 1 signal, which can be made over 250 nm [22]. Meanwhile, Table S3 rows 3,4 give values for $\tilde{m}$ and $d$ for previous MFM studies on superconductors [23, 24].

## V. BACKGROUND SIGNAL

S10 Our primary theoretical result is the calculation of the excess current around a pair of vortices, arising from fused Majoranas in the parity 1 state. We showed that the frequency shift of a magnetic-tipped cantilever due to this excess current is larger than the *noise* in an appropriately designed low-temperature MFM system. Here we compare

the excess current in the parity 1 state to the background *signal* arising from the vortices themselves, and from the stray magnetic field of the tip. Though we will show that the *background* signal is larger than the *parity* signal, we emphasize that the background signal is constant across all vortices, while the excess current in the parity 1 state can be distinguished from the background-only current in the parity 0 state.

### A. Vortex supercurrent

S11 The magnetic field generated by an isolated vortex (without MZM) will produce a much larger signal than the fused Majoranas in the parity 1 state. The supercurrent around the vortices and the resulting perpendicular magnetic field above the surface can be calculated according to Ref. [25] to be

$$j(r,z) = \mu_0 \lambda^{-2}\Big[\frac{\Phi_0}{2\pi\sqrt{r^2+2\xi^2}} - A(r,z)\Big] \tag{S28}$$

$$b_z(r,z) = \frac{\Phi_0}{2\pi\lambda^2}\int_0^\infty dk \frac{kJ_0(k\sqrt{r^2+2\xi^2})}{k^2+\lambda^{-2}} f(k,z) \tag{S29}$$

where

$$A(r,z) = \frac{\Phi_0}{2\pi\sqrt{r^2+2\xi^2}}\int_0^\infty dk \frac{J_1(k\sqrt{r^2+2\xi^2})}{k^2+\lambda^{-2}} f(k,z) \tag{S30}$$

$$f(k,z) = \frac{\tau}{k+\tau}e^{-kz},\ z>0 \tag{S31}$$

$$f(k,z) = 1-\frac{k}{k+\tau}e^{\tau z},\ z\le 0 \tag{S32}$$

$$\tau(k) = \sqrt{k^2+\lambda^{-2}} \tag{S33}$$

and $J_0(x)$ and $J_1(x)$ are Bessel functions. Note this derivation is material-dependent through the penetration depth, $\lambda$, and the coherence length, $\xi$ [26, 27]. The resulting change in cantilever resonance frequency from the vortex supercurrent is several orders of magnitude larger than the excess signal from the parity 1 state, as shown in Fig. S2.

### B. Tip stray magnetic field

S12 The stray field of the MFM tip induces a Meissner response in the underlying superconductor, which generates additional supercurrent around each vortex. To estimate the magnitude of the stray field produced by the Nd coated carbon nanotube on the apex of an AFM tip, we follow the same argument as in Section IV and model the nanotube as a cylinder of radius $a$ and length $L$ with a constant magnetization $M_0$ perpendicular to the sample surface, in the following cylindrical coordinates, the $\hat{\epsilon}$ direction. The magnetic field for a ferromagnetic material can be obtained by

$$\vec{B}^M(\vec{r}) = \frac{\mu_0}{4\pi}\int_V \frac{3(\vec{M}\cdot(\hat{r}-\hat{r'}))(\hat{r}-\hat{r'})-\vec{M}}{(r-r')^3}d\tau' \tag{S34}$$

where in cylindrical coordinates

$$\vec{r} = (L+z)\hat{\epsilon} \tag{S35}$$

$$\vec{r'} = (\rho,\phi,\epsilon) \implies |\vec{r'}| = \sqrt{\rho^2+\epsilon^2} \tag{S36}$$

$$\vec{r''} = \vec{r}-\vec{r'} \implies \hat{r''} = \frac{(-\rho,-\phi,L+z-\epsilon)}{\sqrt{\rho^2+(L+z-\epsilon)^2}} \tag{S37}$$

$$\tag{S38}$$

where $z$ is the tip-sample separation. Defining $\eta = L+z-\epsilon$, taking the dot product with $\hat{\epsilon}$, and plugging in the bounds of integration the stray field becomes

$$\vec{B}^M_\perp = \frac{\mu_0 M_0}{2}\int_\epsilon^{L+\epsilon}\int_0^{R+t}\frac{3\eta^2}{(\rho^2+\eta^2)^{5/2}} - \frac{1}{(\rho^2+\eta^2)^{3/2}}\rho d\rho d\eta \tag{S39}$$

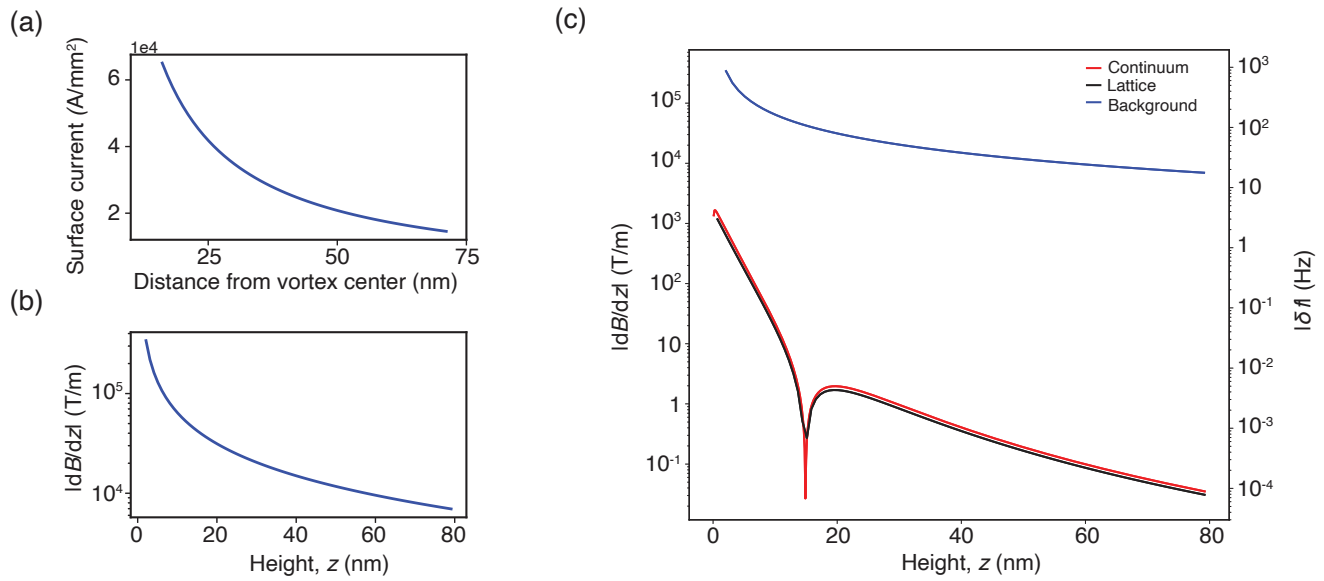


FIG. S2. (a) Current density associated with the background vortex supercurrent as a function of the distance from the vortex center, calculated according to Ref. [25]. (b) Magnetic field gradient associated with the vortex supercurrent above the center of a vortex as a function of tip height, $z$. This is the background magnetic signal in the parity 0 state. (c) Comparison between the magnetic field gradient in (b) from the background vortex (blue) and the excess magnetic field gradient generated by the MZM in the parity 1 state in both the continuum (red) and lattice (black) models, as shown in Fig. 2(c). The corresponding change in resonant frequency of the MFM cantilever tip is calculated via Eq. 6. For these calculations $\lambda = 500$ nm [28, 29] and $\xi = 12$ nm [6], as measured in $FeTe_{0.55}Se_{0.45}$.

where $\eta = L + \epsilon + z$ and the magnetization of Nd is taken to be $M_0 = 4\pi/\mu_0 B_r \sim 1.5 \times 10^7$ A/m where $B_r$ is the remnant field. This integral can be easily evaluated numerically to give the stray field perpendicular to the surface as a function of tip-sample separation, shown in Fig. S3 (b). We choose $a = 6$ nm as we approximate the whole nanotube to be magnetic material for convenience and $L = 250$ nm as reported in Ref. [22].

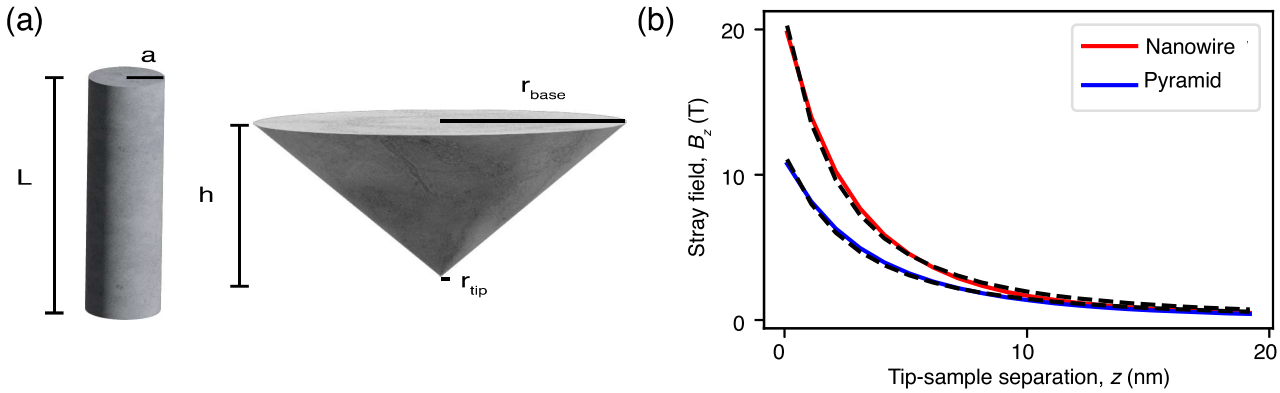


FIG. S3. (a) Conceptual diagram of the two MFM tip geometries considered: a Nd coated carbon nanotube tip (left) and a Nd coated traditional conical tip (pyramid). The dimensions of the tip shapes that are relevant to the equivalent magnetic monopole are labelled: the length $L$, and radius $a$ for the nanotube, and the height $h$, and the base and tip radii, $r_{\text{base}}$ and $r_{\text{tip}}$ for the conical tip. (b) Calculated stray magnetic field of both the Nd coated nanowire (red) and pyramid (blue) from the analytical model given by Eqn. S39 as a function of height above the sample surface. The stray field is calculated where it is the largest on the surface before the Meissner screening, for the point directly beneath the tip, here set as the origin.

## VI. VORTEX-VORTEX REPULSION AND PINNING

**S13** To braid Majoranas, we will need to move vortices easily around each other. But to read Majorana parity, we will need to bring two vortices together so their cores almost touch, overcoming the inter-vortex repulsion, which depends on the dimensionless parameter $\kappa = \lambda/\xi$ [30]. In $FeTe_{0.55}Se_{0.45}$, which is at the extreme type-II limit ($\lambda \sim 500$ nm [28, 29] and $\xi \sim 12$ nm [6] so $\kappa \sim 40$), the vortex-vortex repulsion approaches 100 pN per $\mu$m of film thickness as the separation approaches $2\xi$, as shown in Fig. S4. Therefore, we must strongly pin one vortex while we use the MFM tip to bring another vortex towards it. A promising measurement in ion-irradiated $FeTe_{0.55}Se_{0.45}$ showed how a mixed pinning landscape is created, with the strongest vortex pinning occurring at metallic core columnar defects, then secondary pinning at clusters of point-like defects, followed by collective pinning in relatively clean areas, apparently avoiding poisoning of the MZMs by normal quasiparticles present at the pinning site, and leaving sharp zero bias conductance peak (ZBCP) intact [31].

**S14** Previous MFM measurements using a Si cantilever and optical detection have manipulated and quantified vortex pinning forces in Nb (detecting vortex jumps smaller than 10 nm) [23], cuprates (manipulating vortices with pinning forces from ∼2 to ∼20 pN) [24], and Fe-based superconductors (achieving 500 fN resolution of a 4 pN pinning force) [32]. For initial MZM detection purposes, a tuning fork cantilever may be used, because its higher spring constant $k$ and smaller amplitude noise allows simultaneous STM spectroscopy. Switching from Si to tuning fork cantilevers typically increases $k$ from ∼3 N/m to ∼3000 N/m, so $f_0$ should be increased by the same factor to maintain sensitivity [15, 16]. To lower the noise floor, in situ feedback can be used to increase $Q$ by a factor of up to 20 [33]. Indeed, low-$T$ MFM with a tuning fork has previously shown 2 pN force resolution and 15 nm spatial resolution [34].

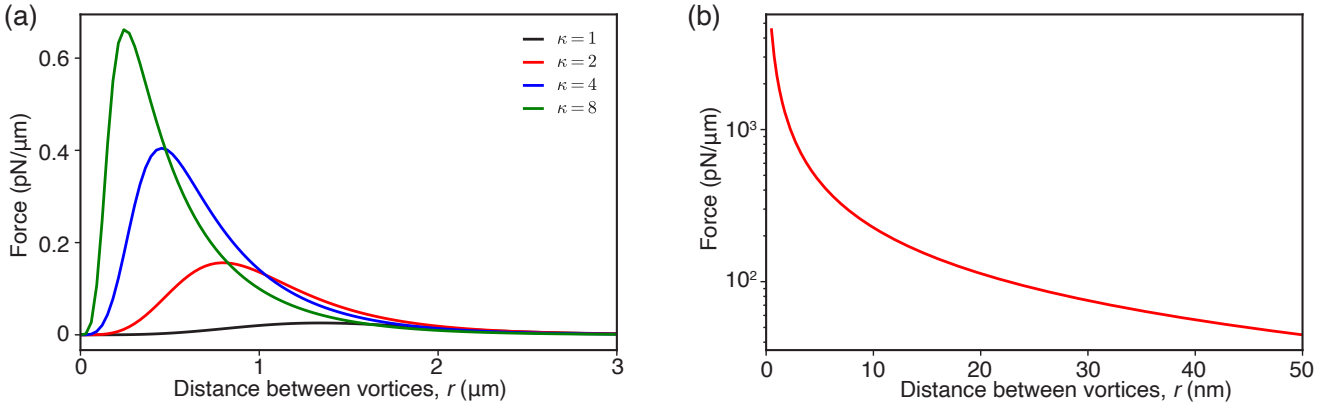


FIG. S4. (a) Inter-vortex repulsion force for increasing values of $\kappa = \lambda/\xi$. As the system approaches the type-II limit, the repulsion force becomes a highly peaked, short range interaction. (b) The infinite $\kappa$ behavior of the vortex-vortex repulsion. This extreme type-II limit well approximates the $FeTe_{1-x}Se_x$ system.


[1] C. Caroli, P. G. de Gennes, and J. Matricon, Bound fermion states on a vortex line in a type II superconducor, Physics Letters **9**, 307 (1964).

[2] N. Hayashi, T. Isoshima, M. Ichioka, and K. Machida, Low-Lying Quasiparticle Excitations around a Vortex Core in Quantum Limit, Physical Review Letters **80**, 2921 (1998).

[3] D. A. Ivanov, Non-Abelian Statistics of Half-Quantum Vortices in p-Wave Superconductors, Physical Review Letters **86**, 268 (2001).

[4] T. Machida, Y. Kohsaka, and T. Hanaguri, A scanning tunneling microscope for spectroscopic imaging below 90 mK in magnetic fields up to 17.5 T, Review of Scientific Instruments **89**, 093707 (2018).

[5] M. Chen, X. Chen, H. Yang, Z. Du, X. Zhu, E. Wang, and H.-H. Wen, Discrete energy levels of Caroli-de Gennes-Matricon states in quantum limit in $FeTe_{0.55}Se_{0.45}$, Nature Communications **9**, 970 (2018).

[6] D. Wang, L. Kong, P. Fan, H. Chen, S. Zhu, W. Liu, L. Cao, Y. Sun, S. Du, J. Schneeloch, R. Zhong, G. Gu, L. Fu, H. Ding, and H. J. Gao, Evidence for Majorana bound states in an iron-based superconductor, Science **362**, 333 (2018).

[7] T. Machida, Y. Sun, S. Pyon, S. Takeda, Y. Kohsaka, T. Hanaguri, T. Sasagawa, and T. Tamegai, Zero-energy vortex bound state in the superconducting topological surface state of Fe(Se,Te), Nature Materials **18**, 811 (2019).

[8] L. Kong, S. Zhu, M. Papaj, H. Chen, L. Cao, H. Isobe, Y. Xing, W. Liu, D. Wang, P. Fan, Y. Sun, S. Du, J. Schnee-

loch, R. Zhong, G. Gu, L. Fu, H.-J. Gao, and H. Ding, Half-integer level shift of vortex bound states in an iron-based superconductor, Nature Physics **15**, 1181 (2019).

[9] S. Zhu, L. Kong, L. Cao, H. Chen, M. Papaj, S. Du, Y. Xing, W. Liu, D. Wang, C. Shen, F. Yang, J. Schneeloch, R. Zhong, G. Gu, L. Fu, Y.-Y. Zhang, H. Ding, and H.-J. Gao, Nearly quantized conductance plateau of vortex zero mode in an iron-based superconductor, Science **367**, 189 (2020).

[10] C. Chen, Q. Liu, W.-C. Bao, Y. Yan, Q.-H. Wang, T. Zhang, and D. Feng, Observation of Discrete Conventional Caroli–de Gennes–Matricon States in the Vortex Core of Single-Layer FeSe/$SrTiO_3$, Physical Review Letters **124**, 097001 (2020), 1905.01850.

[11] Q. Liu, C. Chen, T. Zhang, R. Peng, Y.-J. Yan, C.-H.-P. Wen, X. Lou, Y.-L. Huang, J.-P. Tian, X.-L. Dong, G.-W. Wang, W.-C. Bao, Q.-H. Wang, Z.-P. Yin, Z.-X. Zhao, and D.-L. Feng, Robust and Clean Majorana Zero Mode in the Vortex Core of High-Temperature Superconductor $(Li_{0.84}Fe_{0.16})$OHFeSe, Physical Review X **8**, 041056 (2018).

[12] W. Liu, L. Cao, S. Zhu, L. Kong, G. Wang, M. Papaj, P. Zhang, Y.-B. Liu, H. Chen, G. Li, F. Yang, T. Kondo, S. Du, G.-H. Cao, S. Shin, L. Fu, Z. Yin, H.-J. Gao, and H. Ding, A new Majorana platform in an Fe-As bilayer superconductor, Nature Communications **11**, 5688 (2020).

[13] L. Kong, L. Cao, S. Zhu, M. Papaj, G. Dai, G. Li, P. Fan, W. Liu, F. Yang, X. Wang, S. Du, C. Jin, L. Fu, H.-J. Gao, and H. Ding, Majorana zero modes in impurity-assisted vortex of LiFeAs superconductor, Nature Communications **12**, 4146 (2021).

[14] X. Chen, W. Duan, X. Fan, W. Hong, K. Chen, H. Yang, S. Li, H. Luo, and H.-H. Wen, Friedel Oscillations of Vortex Bound States under Extreme Quantum Limit in $KCa_2Fe_4As_4F_2$, Physical Review Letters **126**, 257002 (2021).

[15] T. R. Albrecht, P. Grütter, D. Horne, and D. Rugar, Frequency modulation detection using high-Q cantilevers for enhanced force microscope sensitivity, Journal of Applied Physics **69**, 668 (1991).

[16] J. Schwenk, S. Kim, J. Berwanger, F. Ghahari, D. Walkup, M. R. Slot, S. T. Le, W. G. Cullen, S. R. Blankenship, S. Vranjkovic, H. J. Hug, Y. Kuk, F. J. Giessibl, and J. A. Stroscio, Achieving $\mu$eV tunneling resolution in an in-operando scanning tunneling microscopy, atomic force microscopy, and magnetotransport system for quantum materials research, Review of Scientific Instruments **91**, 071101 (2020).

[17] Nanosensors AFM Probe SSS-MFMR (2022).

[18] Nanosensors AFM Probe qp-SCONT (2022).

[19] B. W. Chui, Y. Hishinuma, R. Budakian, H. J. Mamin, T. W. Kenny, and D. Rugar, Mass-Loaded Cantilevers with Suppressed Higher-Order Modes for Magnetic Resonance Force Microscopy, TRANSDUCERS '03. 12th International Conference on Solid-State Sensors, Actuators and Microsystems. Digest of Technical Papers (Cat. No.03TH8664) **2**, 1120 (2003).

[20] H. J. Mamin, R. Budakian, B. W. Chui, and D. Rugar, Detection and Manipulation of Statistical Polarization in Small Spin Ensembles, Physical Review Letters **91**, 207604 (2003).

[21] U. Gysin, S. Rast, M. Kisiel, C. Werle, and E. Meyer, Low temperature ultrahigh vacuum noncontact atomic force microscope in the pendulum geometry, Review of Scientific Instruments **82**, 023705 (2011).

[22] Z. Deng, E. Yenilmez, J. Leu, J. E. Hoffman, E. W. J. Straver, H. Dai, and K. A. Moler, Metal-coated carbon nanotube tips for magnetic force microscopy, Applied Physics Letters **85**, 6263 (2004).

[23] E. W. J. Straver, J. E. Hoffman, O. M. Auslaender, D. Rugar, and K. A. Moler, Controlled manipulation of individual vortices in a superconductor, Applied Physics Letters **93**, 172514 (2008).

[24] O. M. Auslaender, L. Luan, E. W. J. Straver, J. E. Hoffman, N. C. Koshnick, E. Zeldov, D. A. Bonn, R. Liang, W. N. Hardy, and K. A. Moler, Mechanics of individual isolated vortices in a cuprate superconductor, Nature Physics **5**, 35 (2009).

[25] G. Carneiro and E. H. Brandt, Vortex lines in films: Fields and interactions, Physical Review B **61**, 6370 (2000).

[26] J. R. Clem, Simple model for the vortex core in a type II superconductor, Journal of Low Temperature Physics **18**, 427 (1975).

[27] J. R. Clem, Two-dimensional vortices in a stack of thin superconducting films: A model for high-temperature superconducting multilayers, Physical Review B **43**, 7837 (1991).

[28] H. Kim, C. Martin, R. T. Gordon, M. A. Tanatar, J. Hu, B. Qian, Z. Q. Mao, R. Hu, C. Petrovic, N. Salovich, R. Giannetta, and R. Prozorov, London penetration depth and superfluid density of single-crystalline $Fe_{1+y}(Te_{1-x}Se_x)$ and $Fe_{1+y}(Te_{1-x}S_x)$, Physical Review B **81**, 180503 (2010).

[29] H. Takahashi, Y. Imai, S. Komiya, I. Tsukada, and A. Maeda, Anomalous temperature dependence of the superfluid density caused by a dirty-to-clean crossover in superconducting $FeSe_{0.4}Te_{0.6}$ single crystals, Physical Review B **84**, 132503 (2011).

[30] A. Chaves, F. M. Peeters, G. A. Farias, and M. V. Milošević, Vortex-vortex interaction in bulk superconductors: Ginzburg-Landau theory, Physical Review B **83**, 054516 (2011).

[31] F. Massee, P. O. Sprau, Y.-L. Wang, J. C. S. Davis, G. Ghigo, G. D. Gu, and W.-K. Kwok, Imaging atomic-scale effects of high-energy ion irradiation on superconductivity and vortex pinning in Fe(Se,Te), Science Advances **1**, e1500033 (2015).

[32] J. T. Zhang, J. Kim, M. Huefner, C. Ye, S. Kim, P. C. Canfield, R. Prozorov, O. M. Auslaender, and J. E. Hoffman, Single-vortex pinning and penetration depth in superconducting $NdFeAsO_{1-x}F_x$, Physical Review B **92**, 134509 (2015).

[33] M. Huefner, A. Pivonka, J. Kim, C. Ye, M. A. Blood-Forsythe, M. Zech, and J. E. Hoffman, Microcantilever Q control via capacitive coupling, Applied Physics Letters **101**, 173110 (2012).

[34] Y. Seo, P. Cadden-Zimansky, and V. Chandrasekhar, Low-temperature high-resolution magnetic force microscopy using a quartz tuning fork, Applied Physics Letters **87**, 103103 (2005).